Proposed Improvements in Response to Referee #1 and 2: Revised Summary

Summary of Manuscript Revisions

To enhance physical robustness and statistical validation, the manuscript has been restructured by applying elements from Information Theory and Wavelet Transform Analysis (based on Mares et al., 2022). This framework allows for the significant separation and quantification of astronomical and radiative variables. Furthermore, discussions have been integrated directly into the results section to improve technical coherence and clarity.

The results obtained through this methodology—utilizing astronomical variables ($LP_0 = D\_au \times \sin(\delta)$), the Bivariate ENSO Timeseries (BEST), and CERES satellite data—provide robust validation for the proposed Relative Geoenergetic Equilibrium (RGE) Hypothesis. Furthermore, the analysis reveals that both radiation (X_I) and astronomical variables (ΔLP) exhibit pure (*PWC*) and synergetic (*MWC*) significance in their coupling with the BEST index. Notably, during the 2005–2010 and 2021–2025 periods, clear synergies are observed in the 8–12-month band (centered at 10 months) and the 2–4-year interannual band, alongside a high-frequency radiative response (1-month band) identified between 2000 and 2015.

These results are consistent across both hemispheres, with particularly strong signals at latitudes N +45.5° and S −45.5°, reinforcing the global validity of the proposed astro-climatic signature. This modulation helps explain recent climate extremes, where the disruption of energetic equilibrium has altered global pressure center dynamics (GPA/LPA). The resulting modulation produces anomalous precipitation and temperature regimes, including extreme snowfall in the Northern Hemisphere and prolonged droughts and wildfires in the Southern Hemisphere, consistent with the empirical satellite evidence presented. Likewise, the *IRGON_Z* index originally proposed in the preprint remains highly consistent with the Information Theory and Wavelet Transform Analysis methodology.

The following points summarize the final structure of the manuscript contents. At the end of this document, the results related to the suggestions by Referee #1 are expanded upon. Some possible adjustments related to the results and epistemology lead to the revised title: "*Astroclimatic signatures in global climate variability and recent extremes: an integrated method and satellite-based evidence of geo-orbital modulation in ENSO.*" Consequently, a new organizational structure has been proposed to provide the clarity and scientific significance these findings merit, focusing on kinematic evidence and information transfer as the primary drivers of the observed associations.

Note: This research adopts an open-system perspective, emphasizing that astro-climatic elements interact dynamically with internal atmospheric and oceanic processes. Our objective is to provide new insights into how orbital geometry modulates observed radiative states, contributing to a more nuanced understanding of the climate system's multi-scale complexity. Consequently, this work does not provide a basis for climate change denial; rather, it seeks to identify the sophisticated mechanisms that bridge external variables with Earth's internal climate dynamics.

2. Materials and Methods

2.1. Net Shortwave Radiation Dataset and Geophysical Proxies (Status: Preprint). The original Merra-ONI databases are maintained as the empirical foundation for net radiation analysis. This provides the historical context for shortwave radiation anomalies and their initial correlation with oceanic indices.

2.2. Satellite Imagery and Sunglint Observations (Status: Preprint). Visual evidence of solar–terrestrial geometry and specular reflection obtained through satellite sensors is utilized. This observational data serves as a qualitative proxy for the angular relationship between the Earth's surface and the solar vector.

2.3. Information Theory and Wavelet Transform Analysis (Status New: PWC–MWC Framework; after Mares et al.) The original cross-correlation analysis has been replaced by a more robust framework involving Multiple Wavelet Coherence (*MWC*) and Partial Wavelet Coherence (*PWC*). This approach isolates pure astronomical signals (ΔLP) from radiative variance (X_I) and quantifies non-linear synergies (S–R). Statistical validation is implemented using AR(1) red-noise models and Monte Carlo simulations, ensuring the results are robust against the serial autocorrelation inherent in the BEST index.

2.4. Spatial Radiative Gradients and Latitudinal Displacement (Status: Preprint + New). The interhemispheric radiative balance is quantified using CERES EBAF satellite data and the Lambert equation at monthly resolution. This section establishes the physical basis of the study, identifying the radiative gradient as the dynamic driver of the system. By analyzing flux at the centers of the Ferrel cells (±45.5°).

2.5. Index of Geo-Orbital Oscillation (IRGON) (Status: Preprint). The definition of the IRGON index is maintained as the primary descriptor of the fundamental geometric oscillation governing the astroclimatic coupling. The index represents the periodic variability in the Earth–Sun position vector, providing a benchmark for the frequency analysis performed in the wavelet domain.

3. Results and Discussion

3.1. Radiative and Geometric Evidence for Astroclimatic Modulation (Status: Preprint). This section provides a descriptive analysis of radiative variability across different ENSO phases, establishing the baseline for observed anomalies in the shortwave spectrum.

3.1.1. Net Downward Shortwave Radiation Variability During ENSO Phases (Status: Preprint). Detailed analysis of how net radiation fluctuates in response to tropical Pacific sea surface temperatures, identifying the characteristic "fingerprints" of radiative forcing during El Niño and La Niña events.

3.1.2. Spatial Radiative Gradients and Latitudinal Displacement (preprint + New semi-empirical model for TOA incoming flux)

The physical formulation for Top of the Atmosphere (TOA) incoming shortwave forcing utilizes Lambert's Law adapted to terrestrial spherical geometry and high-precision NASA and IMCCE ephemerides. The instantaneous solar irradiance (Q) at a specific latitude (φ) is defined by the solar elevation angle (α), following Liou (2002), as:

$$\mathbf{Q = (S_0 / r^2) \cdot \sin(\alpha)}$$

where S_0 is the solar constant (~1361 W/m²), r is the instantaneous Earth–Sun distance (D_{au} in astronomical units), and $\alpha = 90° - \theta_0$ is determined from the solar declination (δ) and observation latitude via the zenith angle θ_0 (Liou 2002, Eq. 2.2.1).

The interhemispheric radiative balance is quantified using CERES EBAF satellite data (Zonal Mean Monthly, Ed4.2) at the Ferrel cell influence area (±45.5°), where millesimal changes in δ alter both intensity and photoperiod duration.

To provide a physically grounded, empirically constrained approximation of the non-recurring character of TOA flux, a diagnostic TOA incoming flux approximation model is proposed. Following a semi-empirical approach analogous to equations of state in physical chemistry (wherein a theoretical base is corrected by empirically fitted terms to account for real-system behavior), the observed monthly TOA flux Q(m,n,t) for the September equinox window at −45.5°S is decomposed for each year as:

$$\mathbf{Q(m,n,t) = [\, I_{pot}(m,t) \cdot \Phi_0(m,n) \,] + [\, \tau(m,n) \cdot t \,] + \Omega_{nr}(m,n,t)}$$

where:

Q(m,n,t) is the semi-empirical model for TOA incoming flux, based on empirical CERES data and NASA/IMCCE ephemerides

$I_{pot}(m,t) = S_0 \cdot \cos(\theta_0) / D_{au}^2$ is the theoretical potential insolation computed from NASA/IMCCE ephemerides at the exact equinox timestamp (Based on Liou 2002, Eq. 2.2.16).

$\Phi_0(m,n)$ is a discrete phase efficiency factor that simultaneously corrects for the Gregorian calendar's quarter-day accumulation and differentiates the four orbital phases (n = N, N+1, N+2, N+3) relative to the CERES EBAF Zonal Mean Monthly baseline.

$\tau(m,n) \cdot t$ is a secular drift term (W/m²/year) quantifying the precession-driven progressive increase in δ at the equinoctial window, with phase-specific slope coefficients (the "secular precession tendency").

$\Omega_{nr}(m,n,t)$ is the non-recurring oscillatory term (W/m²)—the residual between the observed TOA flux and the secular precession tendency. The subscript "nr" denotes its non-recurring character: Ω_{nr} does not exhibit a clear random error structure but rather phase-coherent behavior aligned with the astro-radiative coupling periods identified independently in the PWC/MWC analysis (Section 3.2).

Phase-specific coefficients calibrated against the 2000–2025 CERES EBAF series are provided in Table S-X.

The factor Ω_{nr} exhibits five structurally coherent phases: a positive initial baseline (2000–2003) averaging +0.10 W/m²; a sustained negative drift (2004–2011) deepening to −0.12 W/m²; a transient recovery phase (2012–2014); a profound negative period (2015–2021) reaching −0.15 W/m²; and finally, a positive surge (2022–2025) peaking at +0.21 W/m².

These initial and terminal periods align with the coherence windows independently identified in the Partial and Multiple Wavelet Coherence analysis as significant synergistic phases within the Information Theory framework (Section 3.2).

The behavior of Ω_{nr} in 2024 is particularly revealing: it records its maximum positive value (+0.207 W/m²) precisely when I_{pot} reaches its absolute minimum of the series (944.86 W/m²). This demonstrates that orbital variables—specifically the lateral geometric displacement (ΔLP) driven by the precession-induced drift of δ—complement, compensate, and eventually exceed the reduction in radial irradiance during periods of peak astro-radiative synergy (S–R period 2021–2025).

This decomposition is presented as a complementary semi-empirical framework—not as a replacement for the primary statistical analysis (PWC, NLR, and IRGON), which operates on raw observational and ephemeris data. Its purpose is to provide physical interpretability for the non-recurring character of seasonal radiative states, bridging instantaneous orbital geometry with the observed monthly satellite records at the Top of the Atmosphere.

The complete verification table and phase-specific coefficients are provided in the supplementary material (Table: Non-Recurring Signature and Structural Coherence Phases).

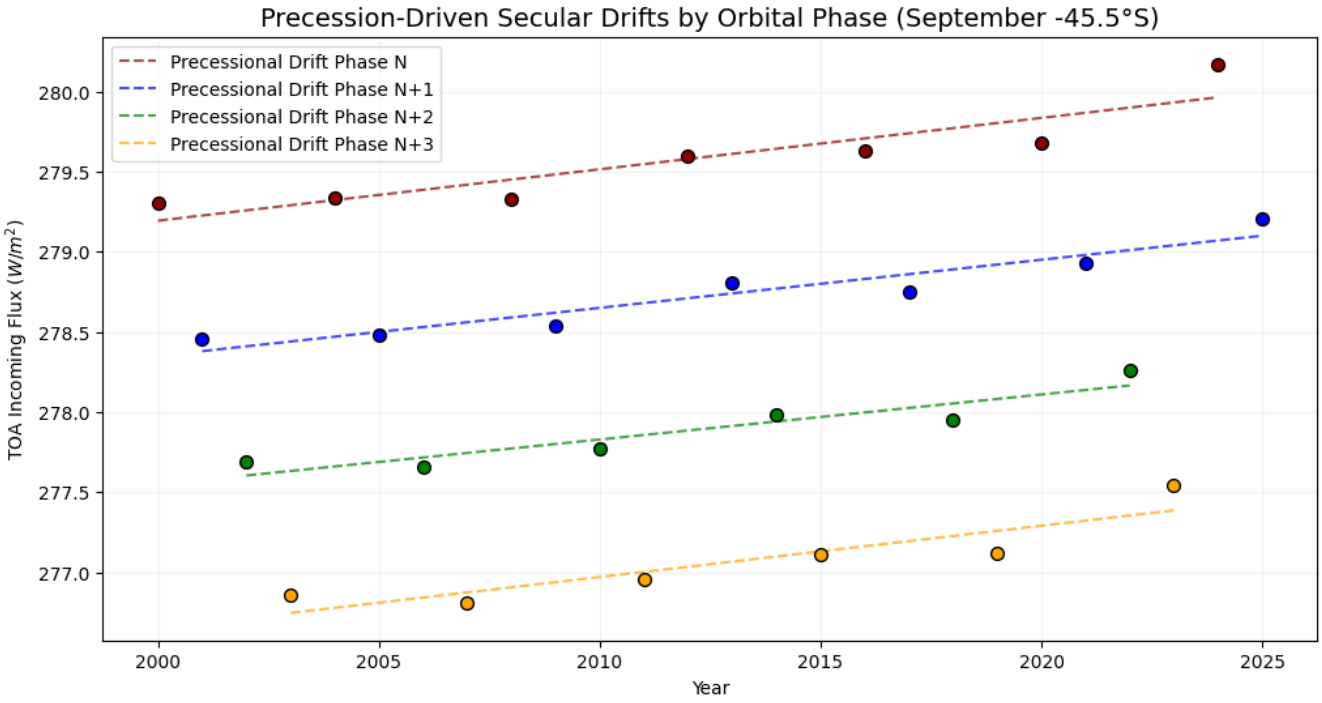
Precession-Driven Secular Drifts by Orbital Phase (September -45.5°S)
Precessional Drift Phase N
Precessional Drift Phase N+1
Precessional Drift Phase N+2
Precessional Drift Phase N+3
TOA Incoming Flux (W/m²)
280.0
279.5
279.0
278.5
278.0
277.5
277.0
2000
2005
2010
2015
2020
2025
Year

105

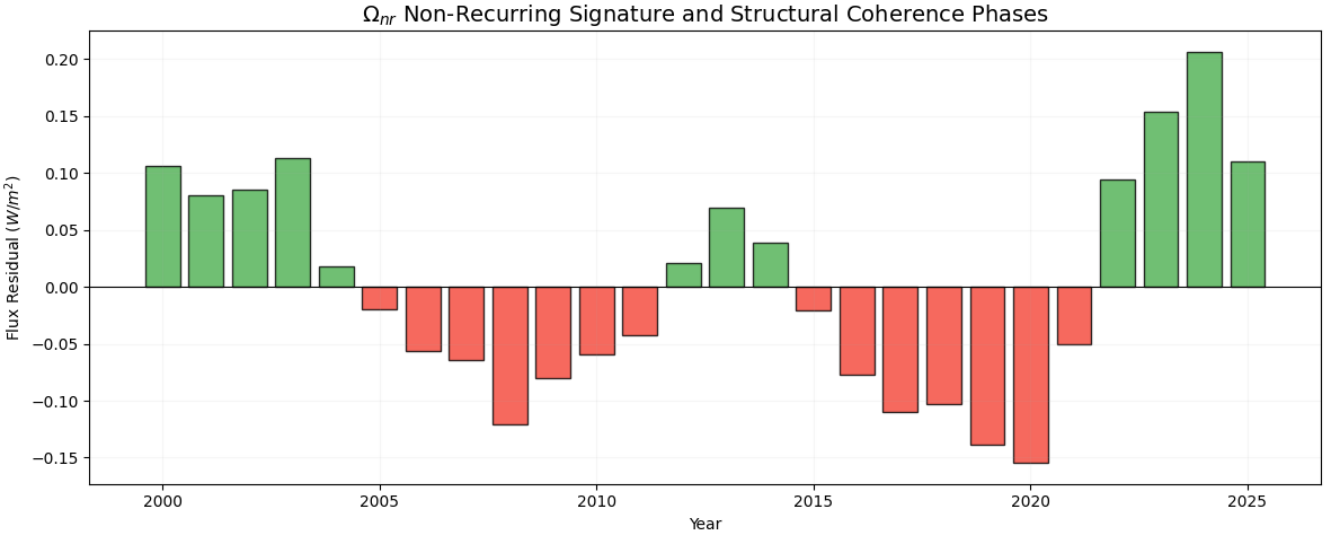
Ωnr Non-Recurring Signature and Structural Coherence Phases
Flux Residual (W/m²)
0.20
0.15
0.10
0.05
0.00
−0.05
−0.10
−0.15
2000
2005
2010
2015
2020
2025
Year

TOA incoming flux approximation model
$Q = [I_{ref} \cdot \Phi_0] + [\tau \cdot t] + \Omega_{nr}$ **(September Equinox -45.5°S)**

Year	Phase	I_{pot}	t	Φ_0	$[I_{ref} \cdot \Phi_0]$	τ	$[\tau \cdot t]$	Q_{mod}	Q_{obs}	Ω_{nr}
2000	N	947.2511	0.0000	0.2947	279.1939	0.0321	0.0000	279.1939	279.3000	0.1061
2001	N+1	947.2264	1.0000	0.2939	278.3500	0.0300	0.0300	278.3800	278.4600	0.0800
2002	N+2	947.1873	2.0000	0.2930	277.5481	0.0281	0.0561	277.6043	277.6900	0.0857
2003	N+3	946.9456	3.0000	0.2922	276.6507	0.0320	0.0960	276.7467	276.8600	0.1133
2004	N	946.9945	4.0000	0.2947	279.1939	0.0321	0.1282	279.3221	279.3400	0.0179
2005	N+1	946.8737	5.0000	0.2939	278.3500	0.0300	0.1500	278.5000	278.4800	-0.0200
2006	N+2	946.6353	6.0000	0.2930	277.5481	0.0281	0.1684	277.7166	277.6600	-0.0566
2007	N+3	946.6130	7.0000	0.2922	276.6507	0.0320	0.2240	276.8747	276.8100	-0.0647
2008	N	946.4437	8.0000	0.2947	279.1939	0.0321	0.2564	279.4504	279.3300	-0.1204
2009	N+1	946.3898	9.0000	0.2939	278.3500	0.0300	0.2700	278.6200	278.5400	-0.0800
2010	N+2	946.3616	10.0000	0.2930	277.5481	0.0281	0.2807	277.8289	277.7700	-0.0589
2011	N+3	946.1170	11.0000	0.2922	276.6507	0.0320	0.3520	277.0027	276.9600	-0.0427
2012	N	946.1142	12.0000	0.2947	279.1939	0.0321	0.3846	279.5786	279.6000	0.0214
2013	N+1	946.0444	13.0000	0.2939	278.3500	0.0300	0.3900	278.7400	278.8100	0.0700
2014	N+2	945.8274	14.0000	0.2930	277.5481	0.0281	0.3930	277.9411	277.9800	0.0389
2015	N+3	945.8334	15.0000	0.2922	276.6507	0.0320	0.4800	277.1307	277.1100	-0.0207
2016	N	945.7096	16.0000	0.2947	279.1939	0.0321	0.5129	279.7068	279.6300	-0.0768
2017	N+1	945.5932	17.0000	0.2939	278.3500	0.0300	0.5100	278.8600	278.7500	-0.1100
2018	N+2	945.5407	18.0000	0.2930	277.5481	0.0281	0.5053	278.0534	277.9500	-0.1034
2019	N+3	945.2846	19.0000	0.2922	276.6507	0.0320	0.6080	277.2587	277.1200	-0.1387
2020	N	945.2503	20.0000	0.2947	279.1939	0.0321	0.6411	279.8350	279.6800	-0.1550
2021	N+1	945.2238	21.0000	0.2939	278.3500	0.0300	0.6300	278.9800	278.9300	-0.0500
2022	N+2	944.9802	22.0000	0.2930	277.5481	0.0281	0.6176	278.1657	278.2600	0.0943
2023	N+3	944.9547	23.0000	0.2922	276.6507	0.0320	0.7360	277.3867	277.5400	0.1533
2024	N	944.8623	24.0000	0.2947	279.1939	0.0321	0.7693	279.9632	280.1700	0.2068
2025	N+1	944.7437	25.0000	0.2939	278.3500	0.0300	0.7500	279.1000	279.2100	0.1100

3.1.3. Satellite Imagery and Sunglint Observations (Status: Preprint). Geometric validation of observation windows through specular reflection (sunglint). These observations confirm the precise solar–terrestrial alignment required for the proposed modulation mechanism.

3.2. Multiscale Oscillatory Coherence and Principal Bands (Status New: After Mares et al.). Following the Referee#1 recommendation, the original Cross-Correlation Function (CCF) has been replaced by an Information Theory and Wavelet Transform framework (Mares et al., 2022). By isolating the pure mutual information (MI) between the geo-orbital oscillation (ΔLP) and the BEST index, we successfully removed redundant solar variance. Statistical significance in the 2–4-year and 10-month bands persists under rigorous AR(1) red-noise modeling and Monte Carlo testing ($p < 0.05$).

3.3. IRGON Model: Geo-Orbital Oscillation Analysis (Status: Preprint + New Figures). Evaluation of the diagnostic capability of the IRGON index to anticipate shifts in global climate dynamics. New figures demonstrate the high degree of phase-locking between the index's geometric oscillations and major shifts in the BEST index.

3.4. The Orbital Differential between Equinoxes (*ΔLP*) (Status: Preprint + New Comments). To address the distance paradox (10^{-4}), we apply the ΔLP component (Lateral Projection of the Earth–Sun position vector). This represents the Earth's spatial displacement relative to the solar equatorial plane at the specific moment of the September equinox. The component is defined as: $LP_0 = D\_au \times \sin(\delta) \times 149{,}597{,}870.7$ Where D_au is the instantaneous Earth–Sun distance in astronomical units, and δ is the solar declination. The resulting ΔLP effectively translates astronomical scales into terrestrial-scale displacements (km).

3.5. Relative Geoenergetic Equilibrium (RGE) Hypothesis (Status: Preprint). This section integrates the findings into a physically plausible mechanism. The RGE hypothesis explains how interannual variations in heliocentric distance and declination—particularly during the September equinox window—are amplified by the latitudinal redistribution of energy. This forces the climate system to adjust its momentum and seek a new equilibrium. This process occurs during periods of significant coupling between astronomical position (ΔLP) and radiative energy (X_1) over open ocean regions, as evidenced by the high synergy observed in the ONI and BEST indices.

DETAILED METHODOLOGY AND RESULTS USING INFORMATION THEORY, ADVANCED WAVELET TRANSFORMS, AND COMPLEMENTARY ORBITAL DYNAMICS

Supplementary tables, multiscale coherence plots, and a supporting bibliography are included to sustain the restructuring of the manuscript. The following sections detail the methodology, results, and discussions of the primary points labeled as Status: New, which significantly strengthen the physical and statistical foundation of the study. The figures and charts are numbered chronologically within this document for clarity, but will be integrated into their respective sections in the final version of the manuscript**.Methods**

3.2. Multiscale Oscillatory Coherence and Principal Bands (Status: New after Mares et al.)

To address the non-linear and non-stationary nature of the climate system, this study adopts the framework proposed by Mares et al. (2022), which integrates Information Theory with advanced Wavelet Transform techniques to isolate the influence of astronomical forcing from radiative variables. Within this methodology, the coupling between the predictors (X_1: radiation; X_2: astronomical variable) and the predictand (Y: BEST index) is evaluated using the Non-linear Correlation Coefficient (*NLR*), derived from Mutual Information (*MI*):

$$\mathrm{NLR} = \sqrt{(1 - \exp(-2MI))} \qquad (1)$$

MI indicates the amount of information shared between two time series, allowing for the detection of dependencies regardless of the statistical distribution of the variables. The dataset comprises a continuous series of 310 months (2000–2025), with seasonal analysis performed on subsets of 78 values per station (e.g., SON). For the Pearson correlation coefficient, confidence levels were determined using standard tables for series of this length. Following the framework of

Mares et al., the 95% confidence levels for the NLR and S–R metrics were established according to the methodologies of Steuer et al. and Theiler et al., ensuring the statistical significance of the non-linear dependencies and synergistic interactions identified.

To further quantify the relative contribution of each predictor, a Synergy–Redundancy (S–R) analysis is implemented following Timme et al. (2014):

$$\text{S–R} = \text{Synergy}\,(Y; X_1, X_2) - \text{Redundancy}\,(Y; X_1, X_2) \quad (2)$$

$$\text{S–R} = MI(X_1, X_2; Y) - MI(X_1; Y) - MI(X_2; Y) \quad (3)$$

A positive S–R value indicates that the combined influence of radiation and orbital kinematics exceeds the sum of their independent contributions, identifying a phase-locked synergy between the variables. Conversely, a negative value implies that the redundant contribution is greater in magnitude than the synergetic contribution. Furthermore, we estimate the Total Correlation (TC) between all variables as:

$$\text{TC} = MI\,(X_1; X_2) + MI\,(X_1, X_2; Y) \quad (4)$$

Where X_1 represents the CERES incoming solar flux (EBAF Ed4.2) at ±45.5° (Ferrel cell mass centers). By selecting this variable as the primary signal, stochastic variability associated with atmospheric processes and oceanic feedbacks is substantially reduced. X_2 corresponds to the astronomical variable defined as the interannual orbital displacement ΔLP ($\Delta LP_n = LP_0(n) - LP_0(n-1)$), where $LP_0 = D\_au \times \sin(\delta)$. The predictand Y represents the Bivariate ENSO Timeseries (BEST) index (Smith and Sardeshmukh, 2000). Astronomical parameters (δ, d) were derived from exact equinox times provided by the Goddard Institute for Space Studies (GISS) and computed using high-precision ephemerides from the IMCCE Solar System Ephemeris Service (J2000). For solstices, ΔLP values were calculated using averaged orbital values to maintain general consistency with the orbital model, while focusing on the equinoctial analysis.

To resolve these interactions in the time–frequency domain, the analysis employs Multiple Wavelet Coherence (*MWC*) to identify the total coherence between both predictors and the climate index. Complementarily, Partial Wavelet Coherence (*PWC*) is applied to isolate the pure astronomical component. As demonstrated by Hu and Si (2021), *PWC* allows for the detection of scale-dependent coherence and lag relationships between two variables while removing the influence of the remaining variables, effectively separating radiative variability from the orbital signal.

The statistical robustness of the results is ensured through several validation procedures. First, AR(1) red-noise modeling is used to account for the serial autocorrelation inherent in the BEST index. Second, Monte Carlo simulations are performed to establish the 95% confidence level, represented by black contour lines in the wavelet coherence plots. Finally, cross-lag optimization is conducted by testing lags months, based on the highest TC and S–R values. This procedure identifies the

operational temporal windows in which the coupled radiation–astronomical system exerts its strongest influence on global energy redistribution.

Results and Discussion

3.2. Multiscale Oscillatory Coherence and Principal Frequency Bands

3.2.1. Comparison of Linear and Non-linear Correlations, Synergy–Redundancy (S–R) and Total Correlation (TC)

Following the methodology of Mares et al. (2022), we first compared the linear (Pearson) and non-linear (NLR) relationships between the astro-radiative predictors and the climate response. The results demonstrate that NLR values are consistently higher than the absolute linear correlation |R| across all analyzed lags (0–10 months), as illustrated in Figure 1. This prevalence of non-linear dependencies aligns with the findings of Le Mouël et al. (2019), who identified robust solar and astronomical signatures across multiple climate indices that are often obscured or attenuated when utilizing strictly linear methods.

For the September equinox (SON), the NLR remains substantially above the 95% confidence level (NLR > 0.25), peaking at lags of 5 and 6 months with values of approximately 0.51 and 0.50, respectively (see Table 1). In contrast, the linear correlation |R| remains consistently near or below the significance threshold (~0.12), with a maximum of only 0.13 at lag 6.

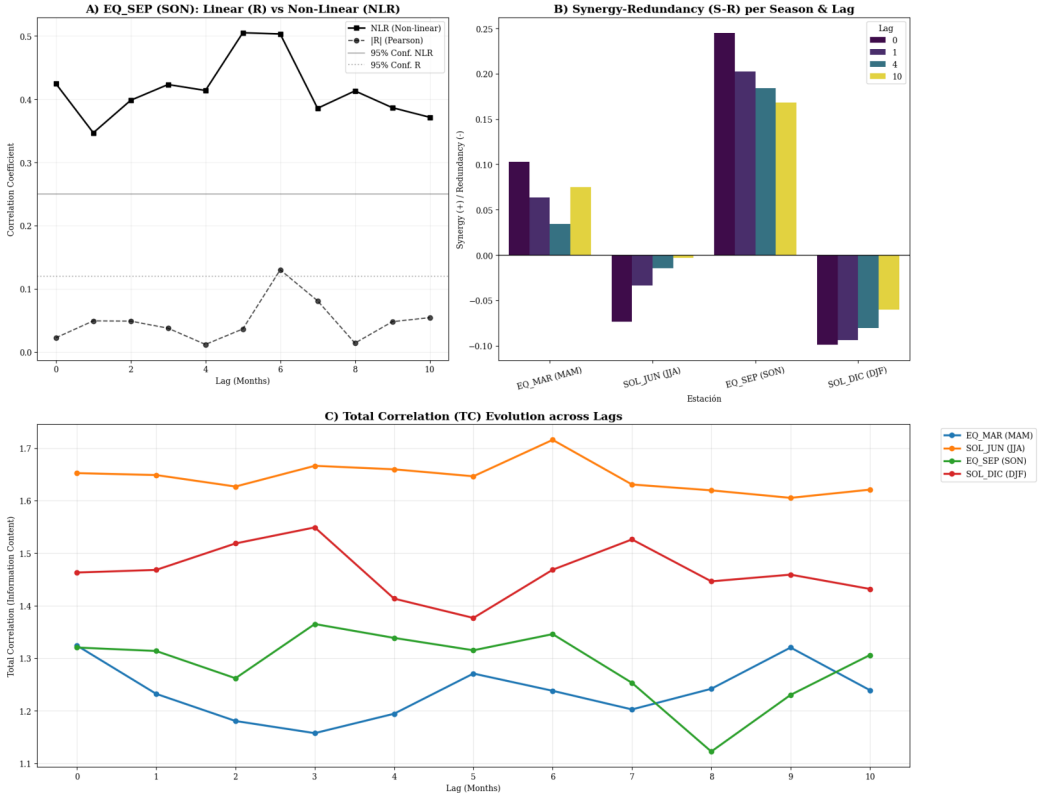

Figure 1 Linear vs. Non-linear Correlation Evolution. Comparison between Pearson |R| and NLR for the SON window across lags 0–10. The shaded area/dashed line represents the 95% confidence interval established via Monte Carlo simulations.

Southern Hemisphere Analysis Summary (-45.5° S)
Synergy-Redundancy (S-R) & Total Correlation (TC)

Season	Metric	Lag 0	Lag 1	Lag 4	Lag 10
EQ_SEP (SON)	S-R	0.2452	0.2027	0.1843	0.1685
	TC	1.3203	1.3137	1.3386	1.2530
	NLR	0.4245	0.3468	0.4138	0.3714
	|R|	0.0227	0.0494	0.0121	0.0546
EQ_MAR (MAM)	S-R	0.1028	0.0636	0.0342	0.0746
	TC	1.3241	1.2321	1.1942	1.1804
SOL_DIC (DJF)	S-R	-0.0987	-0.0939	-0.0805	-0.0600
	TC	1.4631	1.4681	1.4134	1.5261
SOL_JUN (JJA)	S-R	-0.0736	-0.0339	-0.0144	-0.0032
	TC	1.6523	1.6486	1.6595	1.6307

Note: S-R > 0 indicates Synergistic coupling; S-R < 0 indicates Redundancy.

Table 1 Synergy–Redundancy (S–R) and Total Correlation (TC) Metrics. Seasonal values for the equinoctial (SON) and solstitial (JJA, DJF) windows at key lags. Positive S–R denotes synergistic information transfer, while negative values indicate redundancy.

This confirms that the coupling between orbital-geometric perturbations (ΔLP) and the BEST index (Y) is predominantly non-linear and deterministic.

The simultaneous influence of the two predictors (X_1: Radiation and X_2: ΔLP) was evaluated by calculating the difference between synergy and redundancy (S–R) and the Total Correlation (TC) (Table 1):

- **Equinoctial Synergy:** A distinctive feature is observed during the September equinox (EQ_SEP), where S–R reaches its maximum positive value of 0.2452 at lag 0 and remains strongly synergistic at lag 1 (0.2027), as detailed in Table 1. This positive value confirms that the combined action of radiative flux (X_I) and orbital displacement (ΔLP) provides significantly more information about climate variability than each predictor independently, identifying a phase-locked coupling operational window. Based on the maximum TC and S–R peaks, lags of 0, 1, 4, and 10 months were selected for in-depth analysis. Lags 0 and 1 capture the immediate thermodynamic response and the peak of synergistic coupling during the SON window, while lags 4 and 10 months represent the seasonal transition and the nearly annual memory of the system, respectively, aligning with the 10-month oscillatory band identified in the wavelet analysis.

- **Solstitial Redundancy:** Conversely, the solstitial seasons exhibit predominantly negative S–R values. During the June solstice (JJA), redundancy reaches −0.0736 at lag 0, while the December solstice (DJF) shows even greater redundancy, reaching −0.0987. This implies that during solstices, the astronomical signal becomes redundant with the seasonal radiative cycle, providing overlapping rather than synergistic information.

- **Total Dependency:** Maximum TC values exceed 1.70 during the June solstice (JJA) at a 6-month lag. While this indicates a strong total dependency among variables, the negative S–R suggests the system is driven by radiative redundancy during this period, whereas the SON window provides the most efficient information transfer.

These findings validate that the high-coherence patterns identified in the wavelet analysis are not stochastic noise. Instead, they represent a synergistic astroclimatic modulation that peaks during the Southern Hemisphere spring, acting as the primary driver for the redistribution of global geoenergetic equilibrium.

3.2.2 Multi-Scale Wavelet Transform Analysis: MWC and PWC

To detail the time–frequency distribution of these relationships, we applied Multiple Wavelet Coherence (MWC) and Partial Wavelet Coherence (PWC) for the Southern Hemisphere validation at −45.5° S. This multiscale approach isolates the specific contribution of astronomical forcing (ΔLP) across different operational windows.

- **MWC (Synergetic Coupling):** Significant coherent bands are identified in the 2–4 year interannual range and the 8–12 month band, centered at 10 months. The synergy is most evident during the 2005–2010 and 2023–2025 periods, where the combined predictors reach statistical significance, surviving the AR(1) red-noise test (indicated by black contours).

- **PWC Astro (The Pure Signal):** When excluding radiative variance (X_I), a persistent coherent structure remains in the 2–4 year frequency band, particularly evident at lags 4 and 10 months. This "pure" astronomical signal identifies an independent orbital modulation of the global BEST index (Y) that is not merely a reflection of solar flux.

- **Lag Dynamics and Phase-Locking:** The analysis of optimal lags (0, 1, 4, and 10 months) reveals a phase-locked response. At lag 0 and 1, the system shows immediate high-frequency sensitivity. By lag 10, the coherent region in the PWC Astro field becomes broader and more intense, identifying a delayed operational window for the dissipation of the orbital kinematic shock within the Ferrel cell domain.

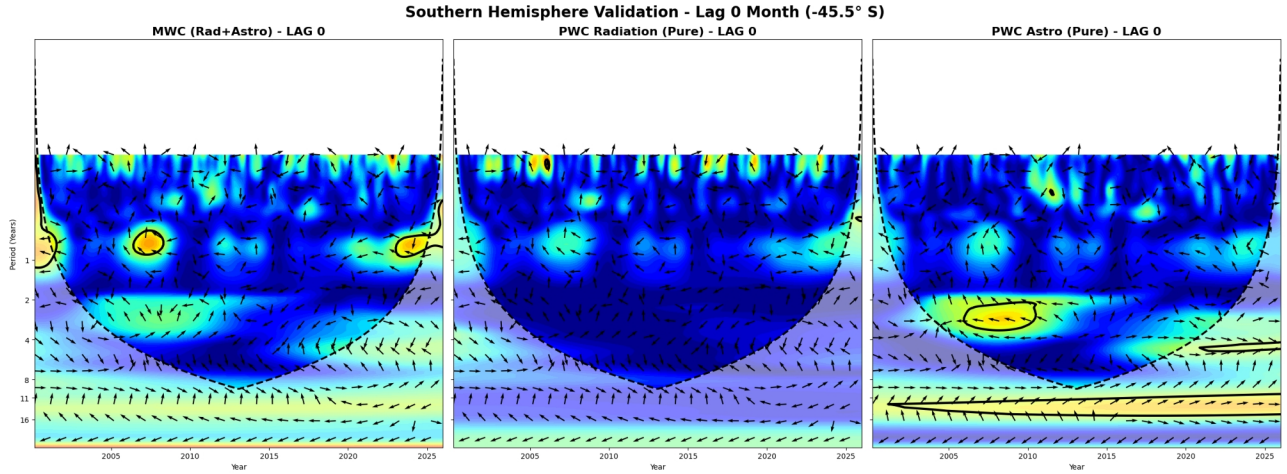

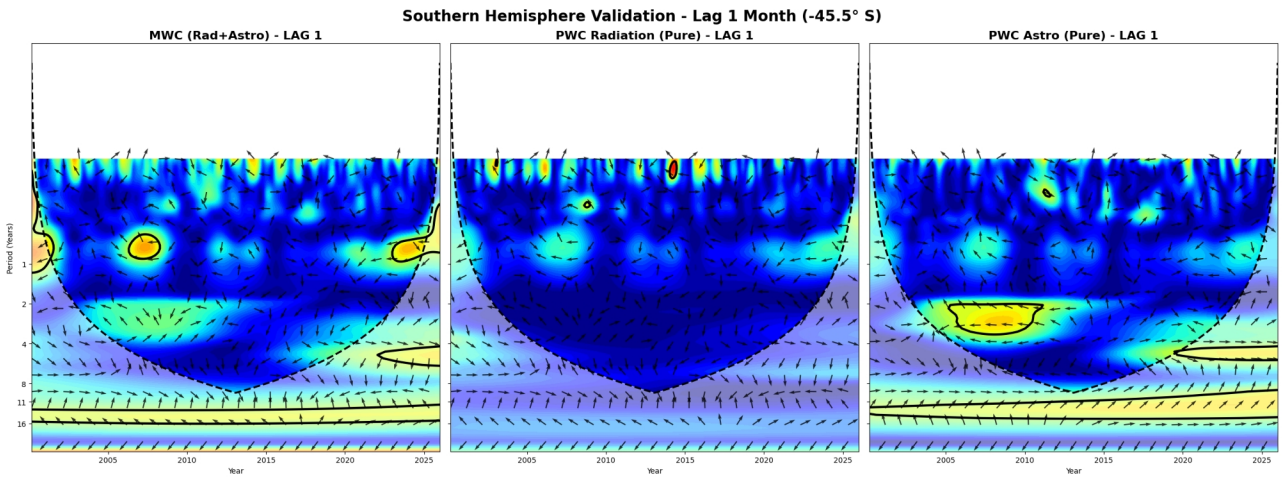

Figure 2 High-Frequency Synergy (Lags 0 & 1) during the SON Season at –45.5° S. MWC and PWC plots showing the immediate coupling during the 2023–2025 period. The black contours denote the 95% confidence level against red noise, validating the synergetic interaction during the September equinox window.

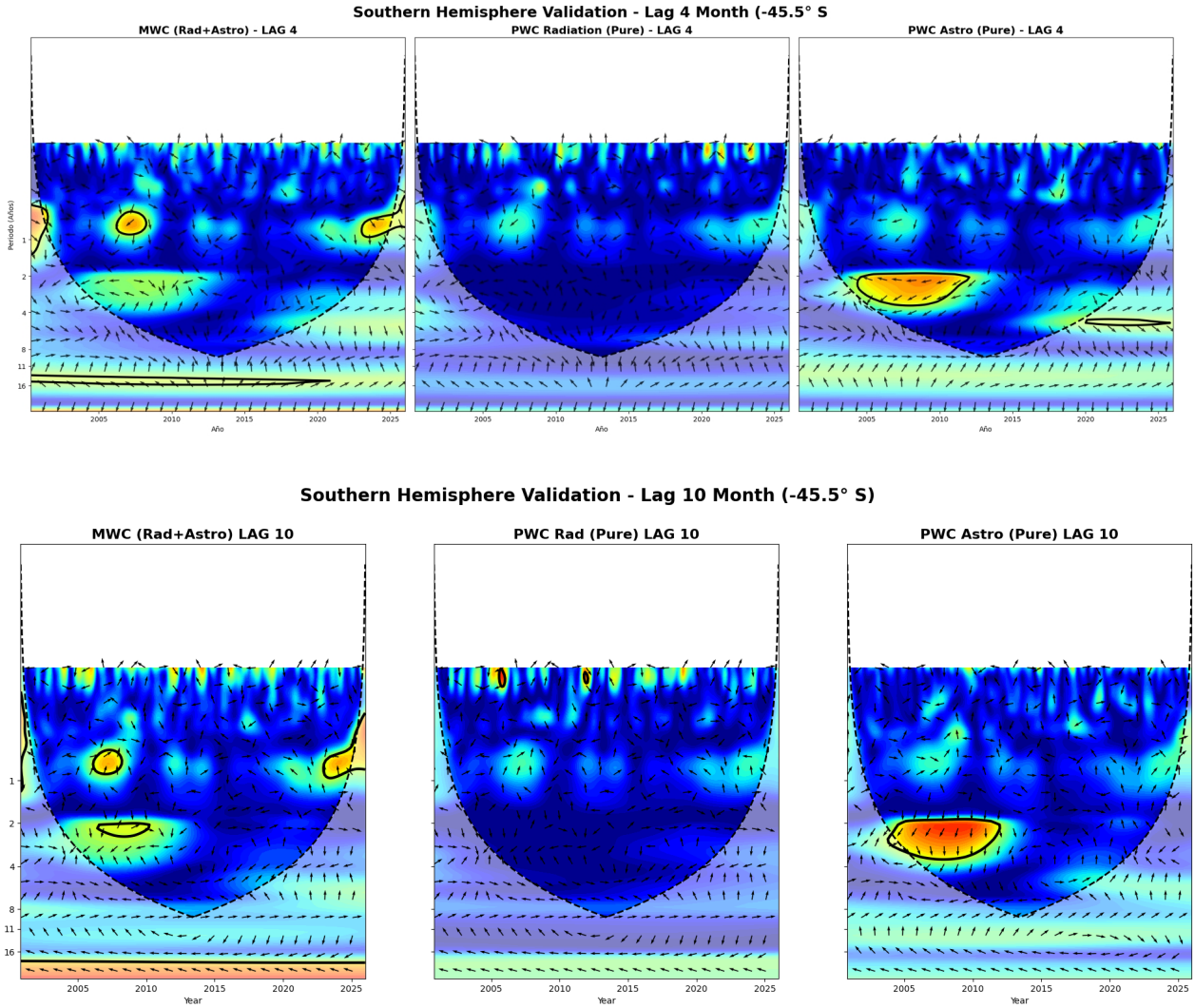

Figure 3 Interannual and 10-month Modulation (Lags 4 & 10) during the SON Season at –45.5° S. At lag 10, the PWC Astro signal (right panel) demonstrates its maximum intensity and breadth in the 2–4 year band, confirming the "pure" astronomical influence of ΔLP on the BEST index (Y) during the spring quarter.

These findings confirm that the recent 2023–2025 anomalies are not stochastic noise but are part of a deterministic phase-locked synergy between radiative energy and orbital kinematics. This modulation, characterized by the 10-month and 2–4

year bands, provides the statistical validation for the Relative Geoenergetic Equilibrium (RGE) hypothesis, suggesting a high-magnitude climate adjustment for the 2026 period.

The application of the MWC–PWC framework to the Northern Hemisphere at +45.5° N confirms the global scale of the identified astro-radiative modulation. The results exhibit high consistency with the Southern Hemisphere patterns, identifying significant coherent structures in the 8–12 month and 2–4 year bands. This interhemispheric symmetry reinforces the hypothesis that the geo-orbital oscillation (ΔLP) acts as a primary driver of the global energy redistribution, with the most intense coupling appearing in phase-locked windows during the 2005–2010 and 2023–2025 periods. The robustness of these results across both hemispheres, surviving the AR(1) red-noise threshold, demonstrates that the identified frequencies are a deterministic feature of the coupled climate system rather than local stochastic variability.

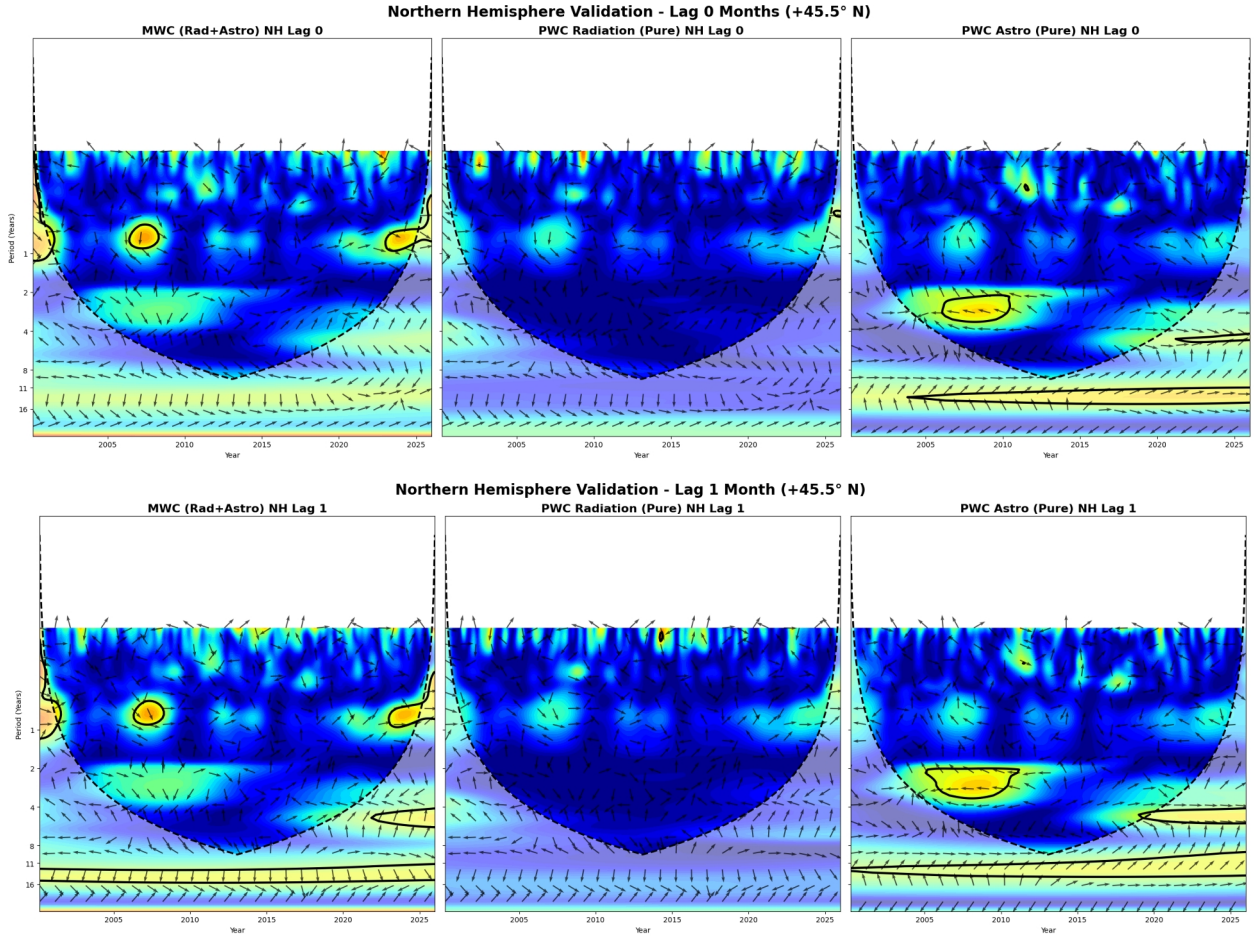

Figure 4 Northern Hemisphere Synergy and Immediate Response (Lags 0 & 1) at +45.5° N**.** MWC and PWC analysis at +45.5° N showing significant phase-locked synergy during the 2023–2025 period. The black contours indicate the 95% confidence level, identifying the radiative and astronomical components' simultaneous influence on the climate index.

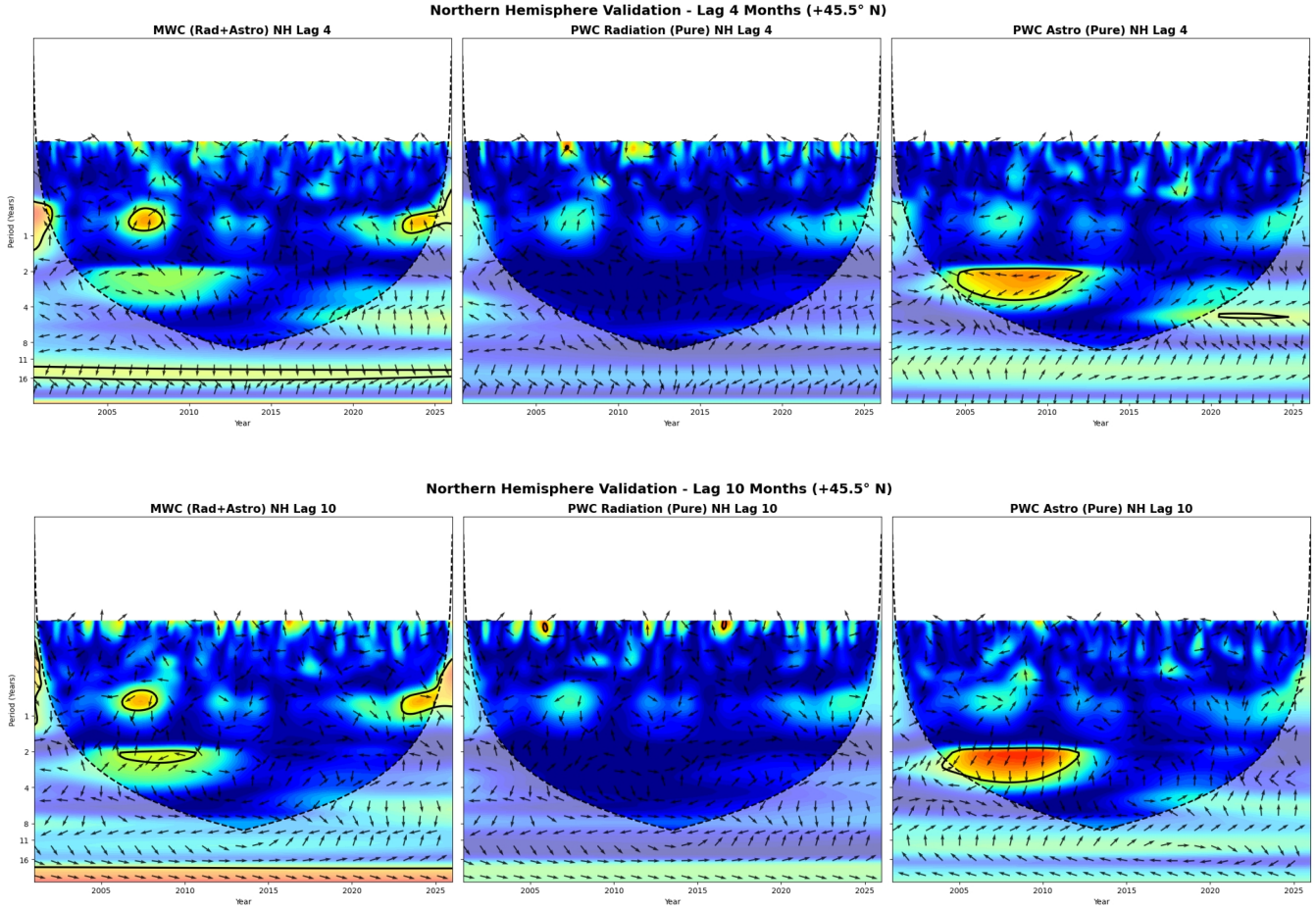

295

Figure 5 Interannual Orbital Modulation in the Northern Hemisphere (Lags 4 & 10) at +45.5° N**.** Consistent with the Southern Hemisphere results, the PWC Astro signal at lag 10 months reveals a broad and persistent significance in the 2–4 year band. This confirms the existence of a "pure" astronomical signal influencing Northern Hemisphere climate dynamics independently of direct radiative variance.

300 **3.3. IRGON Model: Assessing Astroclimatic Oscillatory Periods through Information Theory (Status: Preprint + Added Figure and Commentary)**

The original Wavelet analysis has been replaced with a robust Information Theory framework, following the methodologies established by Mares et al. (2022). This transition is necessitated by the requirement to isolate independent astronomical forcing from complex radiative responses—a task where conventional spectral methods frequently fail to distinguish

between coupled variables. This updated approach quantifies the non-linear coupling and the deterministic Information Flow from geo-orbital parameters to the ocean-atmosphere system, specifically the ONI and BEST indices.

Furthermore, this methodology operates across two levels of information where periodic coherences are observed: the Information Theory analysis utilizes Top of Atmosphere (TOA) or Incoming Flux data at mid-latitudes, while the IRGON model utilizes radiation data specifically at the Open Waters level within the ONI zone. In both cases, the phases and periods remain highly consistent, validating the physical drivers across different atmospheric layers (see Figure 6).

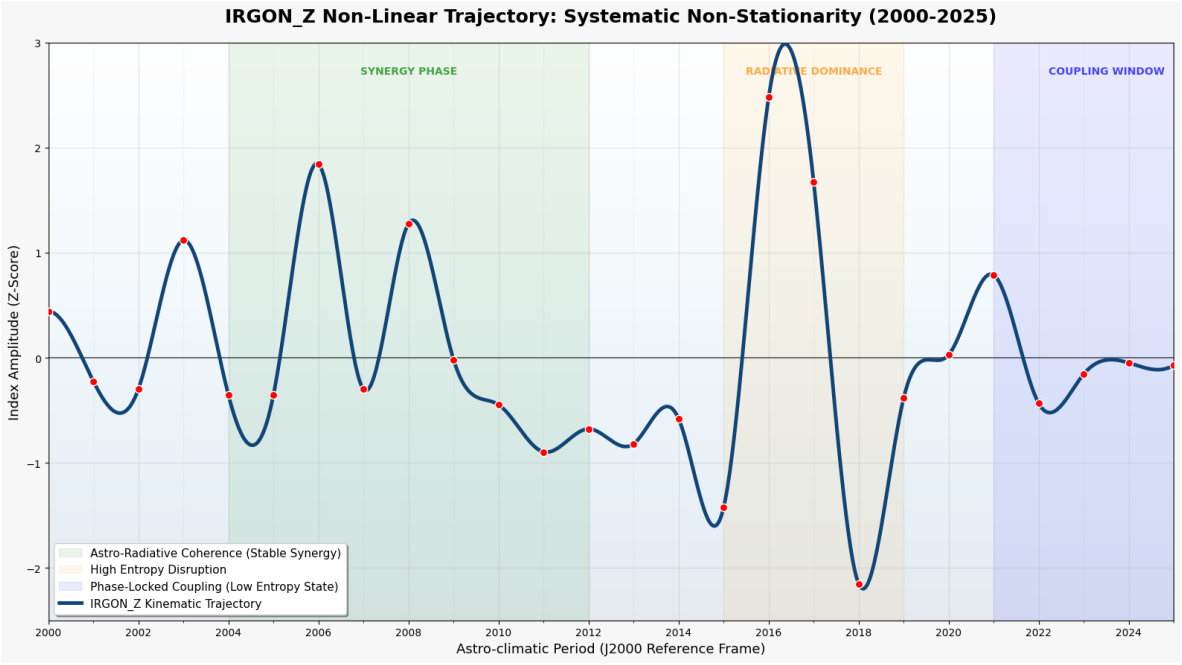

Figure 6. IRGON_Z Non-Linear Oscillation Trajectory: Significance periods derived from Information Theory and Wavelet Transform Analysis.The plot illustrates index frequencies and amplitudes per period, identifying specific intervals of astroclimatic coupling where the orbital signal overrides stochastic noise.

Analyzing the non-linear behavior of the IRGON_Z index through this lens identifies specific patterns of coupling:

- **Identification of Frequency and Amplitude Patterns:** The information-based analysis deconstructs the historical record into distinct physical phases. This reveals clear periods of high informative disruption—such as the 2016 pulse where IRGON_Z reached 2.47—contrasted with phases of low amplitude, as observed in the current 2022–2025 coupling.

- **Validation of Non-Linear periods:** Moving beyond simple linear correlations, Information Theory confirms that IRGON_Z accurately detects when the climate system receives an orbital information pulse strong enough to force

a phase transition. The synergy between orbital distance and solar declination acts as the deterministic driver, establishing a clear cause-and-effect mechanism.

- **The 2024–2025 Lock Phase and the 2026 Trigger:** The analysis detects that during 2024 and 2025, the system entered a period of maximum information transfer and low entropy. This informative stability does not represent inactivity, but rather a significant coupling state period that serves as the precursor to the 2026 trigger.

Finally, a primary mechanism through which these astroclimatic oscillations influence global climate is the modulation of oceanic pressure centers, affecting both their location and magnitude. This is evidenced by analyzing spatial-temporal correlations between Top of the Atmosphere (TOA) incoming shortwave flux from MERRA-2 data and Sea Level Pressure (SLP). These correlations reveal significant shifts in core pressure centers during key periods: September–December 2018 (El Niño), 2022 (La Niña), and 2025 (Neutral-to-Niña transition). These spatial patterns do not contradict the non-linear nature of the system; rather, they represent the atmospheric bridge where deterministic astroclimatic forcing manifests as organized climate responses.

Physically, the 2025 lock or astroclimatic coupling represents a state of minimum entropy. This state is expressed as periods of intensified effects characterized by higher synergy and lower redundancy between astronomical and radiative variables. The high-resolution alignment between TOA flux and surface pressure centers indicates that the climate system has ceased to exhibit relevant stochastic fluctuations. This state of continuous coupling within a specific period facilitates the phase transition observed in early 2026.

As the accumulated geo-orbital energy is released into a new radiative equilibrium, the system undergoes the abrupt shift that characterizes the "Ice and Fire" events of early 2026. This transition is marked by displaced and concentrated pressure centers in critical climatic zones, as documented in the provided imagery. These changes affect multiple areas across mid-latitudes and equatorial regions, displacing the polar effect toward lower latitudes in the Northern Hemisphere (NH), while in the Southern Hemisphere (SH), it significantly reduces precipitation in areas such as the South American Pampas, the Patagonian Andes, and Australia.

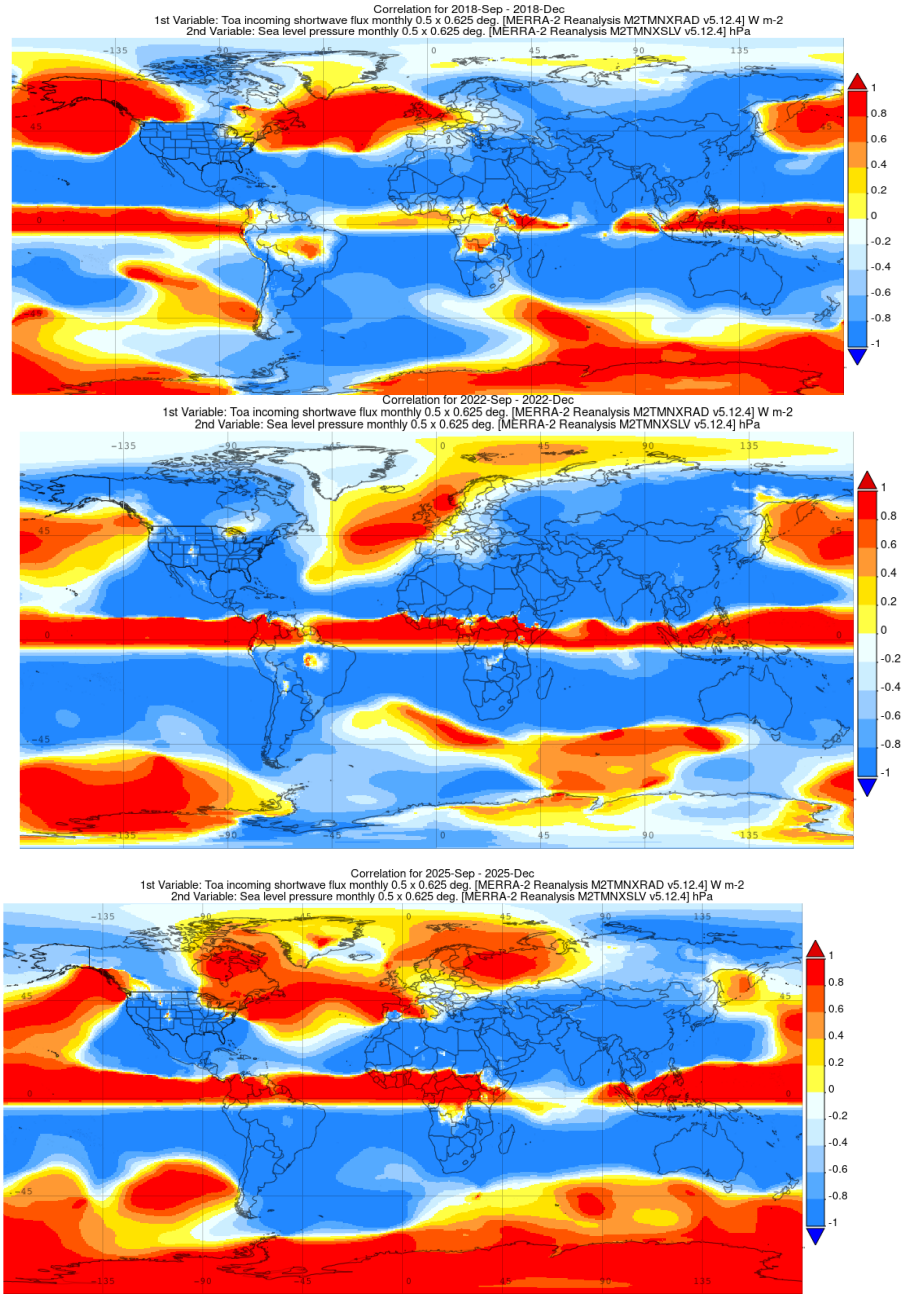

Figure 7 Comparison of atmospheric responses during key astroclimatic windows: (Top) September–December 2018; (Middle) September–December 2022; and (Bottom) September–December 2025. The shifting intensity and location of the core pressure centers demonstrate the atmospheric bridge through which the orbital-geometric coupling forces the 2026 phase transition.

3.4. The Orbital Differential between Equinoxes (Δ*LP*) (Status: NEW)

To address the apparent paradox regarding the small magnitude of astronomical variations (the 10^{-4} scale) and their disproportionate impact on climate, the analytical focus is redefined from gross energy changes to geometric precision. The LP_0 component (lateral projection of the Earth–Sun position vector) is defined as the Earth's spatial displacement relative to the solar equatorial plane at the exact moment of the September equinox (Day 0). This component represents the latitudinal projection of the Earth–Sun vector and is defined as:

$$LP_0 = D\_au \times \sin(\delta) \times 149{,}597{,}870.7 \qquad (5)$$

Where:

- ***D_au*** is the instantaneous Earth–Sun distance in astronomical units (AU).
- ***δ*** (Solar Declination) is the angle relative to the equatorial plane.

Interannual Kinematic Variation. The interannual displacement is defined as the change in Earth's lateral position relative to the solar equatorial plane between consecutive equinoxes:

$$\Delta LP_n = LP_0(n) - LP_0(n-1) \qquad (6)$$

Ephemerides from NASA Horizons and IMCCE show a marked increase in this displacement over the last two decades:

- Year 2000: LP ≈ 8,269 km
- Year 2023: LP ≈ 333,601 km
- Year 2024: LP ≈ 353,509 km
- Year 2025: LP ≈ 360,535 km

Examples of Δ*LP* (Kinematic Magnitude):

1. **Interannual Variation (2023–2024):** Δ*LP* = 353,509 km − 333,601 km = **19,908 km** (This represents the specific annual pulse modulating the current climate state).
2. **Long-term Series Shift (2000–2025):** Δ*LP*_total = 360,535 km − 8,269 km = **352,266 km** (A total displacement comparable to the average distance between the Earth and the Moon, ~384,400 km).

These Δ*LP* values were utilized as the astronomical variable (X_2) in the Partial Wavelet Coherence (PWC) framework, combined with CERES satellite radiation data and the BEST index (Y), producing the statistically significant coherence signals discussed in Section 3.2.

Synchronization Mechanism

This coupling is a fundamental component of the Relative Geoenergetic Equilibrium (RGE) of the climate system, particularly affecting the Ferrel cell domain (±45.5° latitude) and modifying global pressure centers. These dynamical adjustments are consistent with observed anomalies in precipitation and temperature during recent extreme climate events (2023–2025), providing a deterministic link between orbital kinematics, radiative gradients, and large-scale atmospheric circulation variability.

Physical Status and Analytical Decomposition

Δ*LP* is proposed as a kinematic diagnostic index that serves as a proxy for radiative redistribution. Expressed in kilometers (km), this metric quantifies lateral geometric variations across interannual to decadal scales. Rather than acting as a standalone forcing term, Δ*LP* captures the interannual geometric reconfiguration of the Earth-Sun vector, providing a measurable link between orbital dynamics and planetary energy distribution.

The analytical decomposition $LP = \mathrm{D\_au} \cdot \sin(\delta)$ reveals that the observed displacement of ≈ 360,000 km (2000–2025) is the combined result of radial distance (*D_au*) and solar declination (δ). In this relationship, *D_au* acts as a positional factor within the orbital band that scales and amplifies subtle variations, while δ defines the magnitude of change in the lateral vector. This coherent coupling supports the proposed Relative Geoenergetic Equilibrium (RGE) Hypothesis (See Figure 1: *Orbital Window Proxy Scale*).

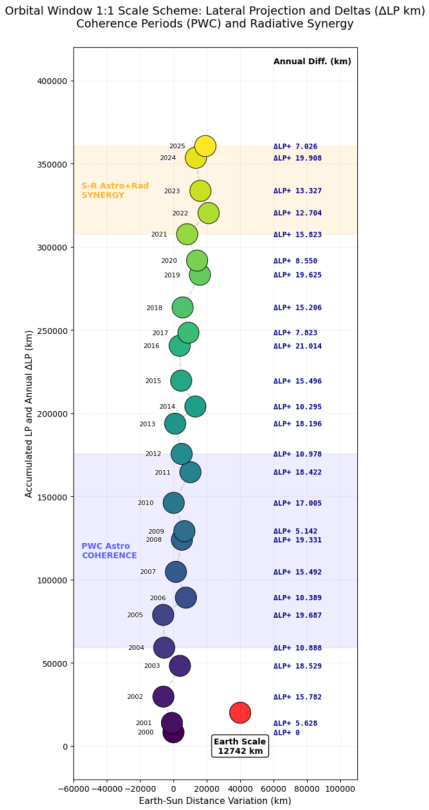

Figure 8 Proxy Scale orbital window scheme: lateral projection (LP) and annual deltas (2000–2025). Earth spheres (d_E ≈ 12,742 km) are plotted by radial distance variation and cumulative lateral displacement. Shaded areas indicate statistical regimes from PWC/MWC: Astro Coherence (2004–2012) and Astro-Radiative Synergy (S-R) (2021–2025). High ΔLP values (e.g., +19,908 km in 2024) correlate with structured radiative anomalies, supporting ΔLP as a kinematic proxy for global energy redistribution and the RGE Hypothesis.

Radiative Mapping and Information Theory

Although the cumulative series reaches 360,000 km, the Information Theory analyses (*PWC/MWC*) utilize interannual differences (Δ*LP*). These values were integrated with the BEST climate index and CERES TOA (incoming flux) radiation data. Geometrically, this displacement modulates the latitudinal distribution of the solar zenith angle, directly affecting radiative gradients over the oceans, particularly at critical latitudes such as 45.5° S and 45.5° N.

The high statistical coherence found through *PWC/MWC* suggests a structured association, where the kinematic state of the orbit preconditions the radiative budget. This reinforces the use of ΔLP as an innovative diagnostic tool for astro-climatic coupling.

Coherence Periods and Climate Dynamics

High-coherence intervals in *PWC* ASTRO and *MWC* S-R coincide with sustained Δ*LP* values exceeding 10,000 km (periods of lower entropy). Conversely, non-significant periods show more frequent low or intermittent ΔLP values. Notably, between 2021 and 2024, ΔLP values were high and increasing, exhibiting a lag of 10 to 12 months.

While the moderating role of the atmosphere and oceans is fundamental, ΔLP oscillations appear to configure significant coupling periods. This dynamics predisposes conditions for climate extremes and phase-shifts in phenomena such as ENSO (e.g., the "Triple-Dip" La Niña 2020–2023), altering pressure centers and precipitation distribution, as evidenced by the "ice and fire" events of early 2026. This approach is not deterministic but proposes a significant coherence based on information transfer and orbital kinematics.

4. Geodynamic Observation:

4.1.The Solsticialization of Equinoxes

An additional descriptive consideration, consistent with the kinematic drift of Δ*LP*, is the gradual trend of the March and September equinoxes toward a geodynamic configuration that resembles "solstice-like behavior" rather than a theoretical perfect equinox. Although these changes appear subtle on solar scales, they represent significant shifts in Earth's energy distribution framework when scaled to planetary dimensions.

Empirical Evidence from CERES (2024 Record): Data from the CERES TOA incoming flux table confirms this trend, with 2024 marking a relevant tipping point. The months adjacent to the September equinox at -45.5° S reached the highest values in the entire 26-year series:

- **August:** 187.90 W/m² (Series maximum).
- **September:** 280.17 W/m² (Series maximum).
- **October:** 383.41 W/m² (Series maximum).

This solsticialization suggests that increased energy coupling in adjacent months during periods of high S-R Synergy pushes the system into new energetic states. This is not necessarily a smooth transition; empirically, many ENSO phases (El Niño/La Niña) initiate or strengthen around the September equinox and undergo phase-shifts near March.

This trend is not restricted to the Southern Hemisphere; CERES data for the Northern Hemisphere (+45.5° N) in 2024 also established a triple record for the March equinox window: March (294.83 W/m²), April (386.77 W/m²), and May (453.78 W/m²); all reached their absolute historical maximums within the CERES series. This parallel behavior with the September records in the Southern Hemisphere confirms the peak in ΔLP synergy (2021–2024).

This solsticialization is a constant process driven by solar declination and precession, yet it manifests significantly in radiative and climate indices during periods of coupling and synergy. This highlights the complexity of the underlying dynamics, evidenced by significant periods of low entropy in the data (e.g., higher coherence and significance). Such patterns are clearly observable in the Precession-Driven Secular Drifts by Orbital Phase plots and data (September -45.5°S), as well as in the oscillations within each Precessional Drift Phase (years N to N+3 of the leap-year orbital order). Consistent results are found across other months, as detailed in the CERES EBAF data provided in the Supplementary Tables.

Coherence and Persistence

The statistical coherence identified in the PWC/MWC analysis aligns with the empirical radiative records discussed above. These results suggest that orbital kinematic states (ΔLP) precondition the synchronization and intensity of interannual climate oscillations through structured periods of synergy between the astronomical variable and net TOA radiation. Within the Information Theory framework applied here, the non-stationary geometric signal (ΔLP) functions as an exogenous structured input to the ocean–atmosphere system — a non-repeating orbital configuration that modulates the system's internal variability.

While the orbital model itself remains effectively invariant at interannual scales, the instantaneous geometric configuration of the Earth–Sun vector exhibits structured, secular non-stationarity when evaluated at climatically critical timestamps (equinox windows). This variability, expressed through the interannual lateral projection delta (ΔLP), defines a non-repeating geometric trajectory that is statistically coherent with observed variations in TOA radiative fluxes (CERES EBAF) and the BEST index across specific frequency bands (2–4 years and 8–12 months), as established through the PWC/MWC framework. Preliminary evidence suggests this geometric non-stationarity extends to solstice windows as well (not yet analyzed in this work, but supported by empirical data), indicating a continuous four-station reconfiguration of the Earth–Sun vector across the seasonal cycle.

The Synergy–Redundancy analysis confirms that this coupling is not reducible to the independent contributions of radiation or orbital kinematics alone: the positive S–R values at the September equinox (EQ_SEP, lag 0: S–R = +0.245) demonstrate that the joint information content of both predictors exceeds their individual contributions, identifying a phase-modulation window. The recent high-coherence interval (2021–2025) displays characteristics comparable to the 2004–2012 PWC astronomical coherence period, suggesting a persistent coupling state rather than an episodic anomaly. These findings are presented not as deterministic causation but as statistically significant evidence of astroclimatic coupling, motivating further investigation into the mutual information structure between orbital kinematics and Earth's radiative energy balance across extended observational records.

New References

Hu, W.; Si, B.C. Multiple wavelet coherence for untangling scale-specific and localized multivariate relationships in geosciences. Hydrol. Earth Syst. Sci. 2016, 20, 3183–3191.

Le Mouël, J.-L., Lopes, F., and Courtillot, V. (2019). A solar signature in many climate indices. *Journal of Geophysical Research: Atmospheres*, 124(5), 2600–2619. https://doi.org/10.1029/2018JD028939

Liou, K. N. (2002). An Introduction to Atmospheric Radiation (2nd ed., Vol. 84). Academic Press.

Mares, C., Dobrica, V., Mares, I., and Demetrescu, C. (2022). Solar Signature in Climate Indices. *Atmosphere*, 13(11), 1898. https://doi.org/10.3390/atmos13111898

Smith, C. A., and Sardeshmukh, P. D. (2000). The Effect of ENSO on the Intraseasonal Variance of Surface Temperature in Winter. *International Journal of Climatology*, 20(13), 1543–1557. https://doi.org/10.1002/1097-0088(20001115)20:13<1543::AID-JOC580>3.0.CO;2-4

Steuer, R., Kurths, J., Daub, C. O., Weise, J., and Selbig, J. (2002). The mutual information: Detecting and evaluating dependencies between variables. *Bioinformatics*, 18(Suppl_2), S231–S240. https://doi.org/10.1093/bioinformatics/18.suppl_2.S231

Theiler, J., Eubank, S., Longtin, A., Galdrikian, B., and Farmer, J. D. (1992). Testing for nonlinearity in time series: The method of surrogate data. *Physica D: Nonlinear Phenomena*, 58(1-4), 77–94. https://doi.org/10.1016/0167-2789(92)90102-S

Timme, N., Alford, W., Flecker, B., and Beggs, J. M. (2014). Synergy, redundancy, and multivariate information measures: An experimentalist's perspective. *Journal of Computational Neuroscience*, 36(2), 119–140. https://doi.org/10.1007/s10827-013-0458-4

TABLES

TABLE 1. Master Astronomical Dataset: September Equinox Kinematic Series (2000–2025)

Year	Deg	Min	Sec	Decl_Dec	Distance_ua	LatProj_AU	LP KM	Delta_LP KM
2000	0	0.0	11.364	0.00316	1.0034954403	0.000055277075	8269	+0
2001	0	0.0	19.102	0.00530	1.0034890839	0.000092898175	13897	+5628
2002	0	0.0	40.784	0.01133	1.0034556370	0.000198395086	29679	+15782
2003	0	1.0	6.241	0.01840	1.0035210213	0.000322251859	48208	+18529
2004	0	1.0	21.205	0.02256	1.0034581238	0.000395034919	59096	+10888
2005	0	1.0	48.252	0.03007	1.0034546587	0.000526633558	78783	+19687
2006	0	2.0	2.521	0.03403	1.0035457601	0.000596075520	89172	+10389
2007	0	2.0	23.812	0.03995	1.0035051237	0.000699634847	104664	+15492
2008	0	2.0	50.364	0.04732	1.0035293325	0.000828858065	123995	+19332
2009	0	2.0	57.432	0.04929	1.0035397645	0.000863230270	129137	+5142
2010	0	3.0	20.803	0.05578	1.0034966610	0.000976900007	146142	+17005
2011	0	3.0	46.091	0.06280	1.0035635465	0.001100040551	164564	+18422
2012	0	4.0	1.192	0.06700	1.0035281871	0.001173423111	175542	+10978
2013	0	4.0	26.195	0.07394	1.0035029572	0.001295057024	193738	+18196
2014	0	4.0	40.312	0.07787	1.0035834094	0.001363873464	204033	+10295
2015	0	5.0	1.621	0.08378	1.0035266610	0.001467457846	219529	+15496
2016	0	5.0	30.504	0.09180	1.0035206983	0.001607931774	240543	+21015
2017	0	5.0	41.232	0.09479	1.0035555204	0.001660223620	248366	+7823
2018	0	6.0	2.134	0.10059	1.0035323731	0.001761866727	263572	+15206
2019	0	6.0	29.071	0.10807	1.0036012399	0.001893053438	283197	+19625
2020	0	6.0	40.825	0.11134	1.0035904943	0.001950208559	291747	+8550
2021	0	7.0	2.582	0.11738	1.0035501402	0.002055980937	307570	+15823
2022	0	7.0	19.991	0.12222	1.0036361286	0.002140900544	320274	+12704
2023	0	7.0	38.324	0.12731	1.0036038239	0.002229987375	333601	+13327
2024	0	8.0	5.682	0.13491	1.0035853090	0.002363062104	353509	+19908
2025	0	8.0	15.312	0.13759	1.0036236121	0.002410029819	360535	+7026

TABLE 2. Master Astronomical Dataset: March Equinox Kinematic Series (2000–2025)

Year	Deg	Min	Sec	Decl_Dec	Distance_ua	LatProj_AU	LP KM	Delta_LP KM
2000	0	0.00	4.78	-0.00133	0.9959600545	-0.0000230901	-3454	+0
2001	0	0.00	21.46	-0.00596	0.9960346004	-0.0001036478	-15505	-12051
2002	0	0.00	37.42	-0.01039	0.9960096381	-0.0001806789	-27029	-11524
2003	0	0.00	51.56	-0.01432	0.9959504466	-0.0002489625	-37244	-10215
2004	0	1.00	13.76	-0.02049	0.9960030673	-0.0003561548	-53280	-16036
2005	0	1.00	30.55	-0.02515	0.9959780387	-0.0004372525	-65412	-12132
2006	0	1.00	56.95	-0.03249	0.9959569810	-0.0005646972	-84478	-19065
2007	0	2.00	11.19	-0.03644	0.9959844653	-0.0006334586	-94764	-10287
2008	0	2.00	25.06	-0.04029	0.9959388106	-0.0007004001	-104778	-10014
2009	0	2.00	53.17	-0.04810	0.9959684427	-0.0008361767	-125090	-20312
2010	0	3.00	13.13	-0.05365	0.9959490681	-0.0009325179	-139503	-14412
2011	0	3.00	33.86	-0.05941	0.9958855971	-0.0010325468	-154467	-14964
2012	0	3.00	57.08	-0.06586	0.9959627709	-0.0011447556	-171253	-16786
2013	0	4.00	14.16	-0.07060	0.9959640057	-0.0012272386	-183592	-12339
2014	0	4.00	38.09	-0.07725	0.9959147699	-0.0013426860	-200863	-17271
2015	0	4.00	55.27	-0.08202	0.9959470022	-0.0014257118	-213283	-12420
2016	0	5.00	9.71	-0.08603	0.9959065880	-0.0014953792	-223706	-10422
2017	0	5.00	36.01	-0.09334	0.9959360977	-0.0016223871	-242706	-19000
2018	0	5.00	51.78	-0.09772	0.9959536299	-0.0016985709	-254103	-11397
2019	0	6.00	3.53	-0.10098	0.9958742635	-0.0017551902	-262573	-8470
2020	0	6.00	25.99	-0.10722	0.9959189540	-0.0018637039	-278806	-16233
2021	0	6.00	44.66	-0.11241	0.9959060141	-0.0019538092	-292286	-13480
2022	0	7.00	12.79	-0.12022	0.9958232114	-0.0020894598	-312579	-20293
2023	0	7.00	36.16	-0.12671	0.9958748777	-0.0022024015	-329475	-16896
2024	0	7.00	50.46	-0.13068	0.9958642583	-0.0022714388	-339802	-10328
2025	0	8.00	19.55	-0.13876	0.9958887671	-0.0024119371	-360821	-21018

Note: As specified in the manuscript, the astronomical data originates from **NASA** time standards and ephemeris data from the **IMCCE (Paris Observatory)**.

TABLE 3. CERES TOA Incoming Solar Flux (45.5° S) EBAF Ed4.2 (2000-2025) W/m^2

Year	JAN	FEB	MAR	APR	MAY	JUN	JUL	AUG	SEP	OCT	NOV	DEC
2000	--	--	319.83	218.04	143.82	112.18	127.32	187.41	279.30	382.89	470.02	512.43
2001	492.24	420.60	320.74	218.72	144.29	112.27	127.05	186.74	278.46	381.99	469.34	512.26
2002	492.78	421.44	321.75	219.50	144.72	112.36	126.70	186.08	277.69	381.12	468.73	512.16
2003	493.00	422.04	322.40	220.17	145.11	112.37	126.40	185.46	276.86	380.00	468.07	511.85
2004	493.17	420.99	319.71	217.87	143.73	112.15	127.28	187.34	279.34	382.71	469.78	512.13
2005	491.77	420.20	320.51	218.56	144.13	112.19	127.00	186.74	278.48	381.88	469.15	511.90
2006	492.21	420.93	321.35	219.29	144.61	112.28	126.70	186.07	277.66	381.02	468.51	511.72
2007	492.57	421.63	322.21	220.02	145.01	112.35	126.40	185.46	276.81	380.18	467.99	511.64
2008	493.00	420.78	319.51	217.71	143.64	112.11	127.32	187.40	279.33	382.66	469.70	511.95
2009	491.70	420.06	320.37	218.44	144.08	112.19	127.03	186.78	278.54	381.86	469.14	511.82
2010	492.11	420.87	321.29	219.23	144.55	112.28	126.76	186.20	277.77	381.10	468.65	511.77
2011	492.58	421.62	322.15	220.02	145.02	112.37	126.47	185.58	276.96	380.39	468.25	511.89
2012	493.14	420.88	319.53	217.72	143.64	112.15	127.40	187.58	279.60	382.93	469.98	512.17
2013	491.80	420.11	320.39	218.42	144.09	112.24	127.15	186.97	278.81	382.09	469.36	512.10
2014	492.21	420.79	321.38	219.24	144.55	112.31	126.85	186.36	277.98	381.26	468.92	512.02
2015	492.79	421.86	322.25	220.01	144.99	112.39	126.57	185.70	277.11	380.56	468.35	511.87
2016	493.10	420.82	319.47	217.59	143.58	112.15	127.45	187.62	279.63	382.95	469.94	512.04
2017	491.69	419.96	320.22	218.31	144.01	112.20	127.14	186.97	278.75	382.14	469.35	511.91
2018	492.05	420.64	321.05	219.04	144.44	112.27	126.84	186.35	277.95	381.29	468.75	511.80
2019	492.48	421.43	321.93	219.75	144.86	112.33	126.54	185.71	277.12	380.46	468.19	511.70
2020	492.90	420.58	319.26	217.47	143.50	112.12	127.47	187.68	279.68	382.99	469.94	512.11
2021	491.71	419.93	320.18	218.25	143.96	112.21	127.21	187.11	278.93	382.27	469.49	512.09
2022	492.26	420.89	321.20	219.12	144.50	112.36	126.97	186.55	278.26	381.68	469.15	512.08
2023	492.80	421.77	322.23	219.95	144.94	112.45	126.68	186.00	277.54	381.06	468.76	512.21
2024	493.37	420.83	319.50	217.64	143.59	112.24	127.66	187.90	280.17	383.41	470.44	512.57
2025	492.09	420.19	320.43	218.37	144.01	112.30	127.36	187.31	279.21	382.58	469.86	512.23

TABLE 4. CERES TOA Incoming Solar Flux (+45.5° N) EBAF Ed4.2 (2000-2025) W/m^2

Year	JAN	FEB	MAR	APR	MAY	JUN	JUL	AUG	SEP	OCT	NOV	DEC
2000	--	--	293.96	385.94	453.16	481.51	464.67	406.78	322.12	229.53	154.02	120.01
2001	139.18	203.26	293.21	385.23	452.89	481.52	465.11	407.25	322.80	230.19	154.43	120.06
2002	138.86	202.64	292.61	384.66	452.48	481.54	465.19	407.75	323.57	230.84	154.88	120.14
2003	138.46	201.90	291.65	383.88	451.94	481.22	465.45	408.31	324.29	231.39	155.32	120.17
2004	138.04	202.60	294.04	385.92	453.10	481.34	464.34	406.36	321.93	229.29	153.86	119.93
2005	139.11	203.20	293.22	385.19	452.63	481.23	464.69	406.97	322.59	229.96	154.31	119.97
2006	138.77	202.53	292.44	384.53	452.34	481.24	464.99	407.47	323.32	230.63	154.74	120.03
2007	138.39	201.84	291.68	383.85	451.84	481.13	465.24	408.05	324.00	231.31	155.22	120.12
2008	138.05	202.63	294.05	385.90	453.06	481.23	464.27	406.20	321.69	229.10	153.76	119.89
2009	139.16	203.26	293.28	385.23	452.69	481.22	464.61	406.81	322.44	229.80	154.23	119.95
2010	138.80	202.63	292.57	384.68	452.38	481.26	465.00	407.46	323.23	230.53	154.71	120.03
2011	138.46	201.96	291.82	384.10	452.09	481.30	465.31	408.03	323.97	231.29	155.23	120.17
2012	138.15	202.81	294.27	386.15	453.28	481.44	464.33	406.33	321.79	229.11	153.78	119.93
2013	139.25	203.42	293.50	385.44	452.94	481.47	464.83	406.95	322.54	229.80	154.22	120.01
2014	138.89	202.73	292.86	384.94	452.62	481.44	465.08	407.56	323.25	230.50	154.73	120.09
2015	138.58	202.20	292.09	384.33	452.25	481.39	465.46	408.04	323.92	231.24	155.18	120.15
2016	138.21	202.91	294.40	386.17	453.31	481.42	464.32	406.16	321.59	228.98	153.70	119.90
2017	139.28	203.48	293.54	385.51	452.90	481.34	464.57	406.68	322.24	229.68	154.14	119.96
2018	138.90	202.77	292.76	384.83	452.49	481.27	464.88	407.25	322.99	230.34	154.59	120.03
2019	138.55	202.13	292.01	384.15	452.05	481.18	465.14	407.79	323.70	231.04	155.06	120.11
2020	138.21	202.92	294.41	386.21	453.29	481.32	464.19	406.02	321.44	228.86	153.63	119.91
2021	139.35	203.59	293.71	385.64	452.98	481.40	464.63	406.69	322.23	229.61	154.12	120.00
2022	139.02	203.03	293.08	385.23	452.91	481.67	465.15	407.43	323.14	230.44	154.65	120.10
2023	138.71	202.41	292.47	384.73	452.52	481.71	465.44	408.14	323.96	231.25	155.17	120.22
2024	138.40	203.17	294.83	386.77	453.78	481.83	464.68	406.20	321.78	228.95	153.71	120.01
2025	139.52	203.85	294.13	386.12	453.39	481.80	464.97	406.89	322.33	229.64	154.16	120.02

TABLE 5. BEST INDEX (BIVARIATE ENSO STATE) SERIES: 2000-2025

Year	JAN	FEB	MAR	APR	MAY	JUN	JUL	AUG	SEP	OCT	NOV	DEC
2000	--	--	-1.20	-1.06	-0.66	-0.39	-0.16	-0.43	-0.61	-0.74	-1.32	-0.67
2001	-0.81	-0.97	-0.46	-0.12	0.31	0.00	0.32	0.41	-0.17	0.06	-0.44	0.33
2002	-0.15	-0.34	0.49	0.37	0.96	0.94	0.93	1.23	0.96	1.01	1.05	1.35
2003	0.74	0.91	0.79	0.23	0.01	0.29	0.15	0.18	0.24	0.42	0.43	-0.20
2004	0.88	-0.33	0.08	0.64	-0.22	0.65	0.80	0.86	0.73	0.58	0.79	0.88
2005	0.25	1.87	0.35	0.72	1.03	0.23	0.12	0.33	-0.14	-0.54	-0.04	-0.22
2006	-1.14	-0.32	-0.98	-0.51	0.47	0.40	0.52	0.99	0.82	1.21	0.50	0.83
2007	0.82	0.31	0.12	0.11	0.02	-0.15	0.06	-0.43	-0.69	-1.06	-1.21	-1.45
2008	-1.59	-2.10	-1.18	-0.90	-0.27	-0.45	-0.01	-0.37	-0.75	-0.72	-0.88	-0.98
2009	-1.19	-1.64	-0.36	-0.54	0.66	0.68	0.59	0.95	0.30	1.77	1.44	1.67
2010	1.53	1.72	1.25	-0.18	-0.75	-0.70	-2.02	-2.29	-2.57	-2.21	-1.79	-2.66
2011	-2.30	-2.58	-2.22	-1.71	-0.63	-0.31	-0.82	-0.79	-1.15	-1.04	-1.40	-2.09
2012	-1.11	-0.67	-0.73	-0.01	-0.06	0.43	0.52	0.63	0.22	-0.06	0.01	0.41
2013	-0.09	-0.05	-0.98	-0.12	-0.76	-0.93	-0.71	-0.33	-0.18	-0.07	-0.55	0.83
2014	-1.08	-0.28	0.59	-0.16	0.09	0.38	0.36	0.64	0.87	0.75	1.22	0.83
2015	0.94	0.20	0.86	0.91	1.69	1.53	2.30	2.45	2.63	2.53	1.75	1.72
2016	2.82	2.60	1.23	1.75	0.19	-0.27	-0.42	-0.87	-1.08	-0.24	-0.19	-0.38
2017	-0.22	0.05	-0.57	0.39	0.20	0.51	-0.31	-0.51	-0.71	-0.93	-1.12	-0.27
2018	-1.07	-0.08	-1.35	-0.51	-0.26	0.25	0.15	0.27	0.96	0.25	0.60	-0.11
2019	0.38	1.34	0.83	0.59	1.05	0.91	0.76	0.25	1.01	0.62	1.10	0.70
2020	0.30	0.36	0.41	0.41	-0.32	0.10	-0.24	-1.09	-0.99	-1.02	-1.01	-1.61
2021	-1.72	-1.56	-0.66	-0.59	-0.62	-0.23	-1.12	-0.70	-0.81	-0.96	-1.19	-1.46
2022	-0.63	-1.12	-1.62	-1.73	-1.98	-1.61	-0.95	-1.45	-1.79	-1.78	-0.60	-1.75
2023	-1.23	-1.29	-0.13	0.14	1.44	0.77	1.29	1.77	2.12	1.29	1.70	1.15
2024	0.65	1.85	0.62	1.01	0.10	0.27	0.85	-0.63	0.11	-0.47	-0.38	-0.97
2025	-0.43	-0.58	-0.96	-0.31	-0.27	-0.10	-0.37	-0.38	-0.51*	-1.21*	-0.95*	-0.97*

CLARIFICATION: SEPTEMBER TO DECEMBER 2025 VALUES (MARKED WITH *) WERE CALCULATED

Summary Technical Notes

1. Data Provenance & Astronomical Alignment.

All astronomical datasets, NASA time standards, and ephemeris data used in this manuscript originate from NASA and the IMCCE (Paris Observatory), respectively. This ensures kinematic precision for equinox and solar flux positioning. Refer to the manuscript for specific orbital parameterizations.

2. Incoming Solar Flux Data (CERES EBAF Ed4.2)

Data Origin and Sources Incident solar radiation data at the Top of the Atmosphere (TOA) is sourced from NASA's CERES (Clouds and the Earth's Radiant Energy System) project.

- Official Source: CERES EBAF-TOA Ed4.2 Data Tool
- Parameters: TOA Fluxes and Solar Flux (Zonal Mean).
- Time Range: March 2000 to December 2025.
- Astronomical Context: As noted in the manuscript, these records are aligned with NASA time standards and ephemeris data from the IMCCE (Paris Observatory).

Dataset Specifications Historical and projected series were processed for specific latitudes (±45.5° N/S) to analyze incoming solar flux variability:

3. Latitude +45.5° N

4. Latitude -45.5° S

3. BEST Index Calculation (Sep-Dec 2025)

This note clarifies the methodology used to calculate the BEST Index (Bivariate ENSO State Index) for the period of September to December 2024, based on official NOAA/CPC data.

Primary Data Sources

- SST 3.4 (CPC/NOAA): ERSST.v5 Niño 3.4 Index
- SOI (CPC/NOAA): Southern Oscillation Index

Official Bivariate Formula

To ensure high technical accuracy, the index is calculated using the bivariate normalization of oceanic and atmospheric signals:

BEST = [(SST_Anomaly / σ_SST) - (SOI / σ_SOI)] × (Scale_Factor / 2)

Standardization Parameters (1981-2010 Climatology):

- SST Deviation (σ): 0.92
- SOI Deviation (σ): 1.62
- Scale Factor: 1.75 (Adjusted to normalize bivariate amplitude).

Step-by-Step Validation (September 2025 Example)

Using the official observed inputs for September:

- Niño 3.4 SST Anomaly: -0.48 (Cooling ocean)
- SOI Index: +0.10 (Neutral/Cooling atmosphere)

Calculation Process:

- Ocean Normalization: -0.48 / 0.92 = -0.521
- Atmosphere Normalization: +0.10 / 1.62 = 0.061
- Signal Difference: -0.521 - 0.061 = -0.582 *(Note: SOI is subtracted because a positive SOI value indicates cooling, consistent with a negative SST).*
- Applying Scale Factor: (-0.582 / 2) × 1.75 = -0.509
- Final Result for September 2025: -0.51